Provided for non-commercial research and education use.
Not for reproduction, distribution or commercial use.

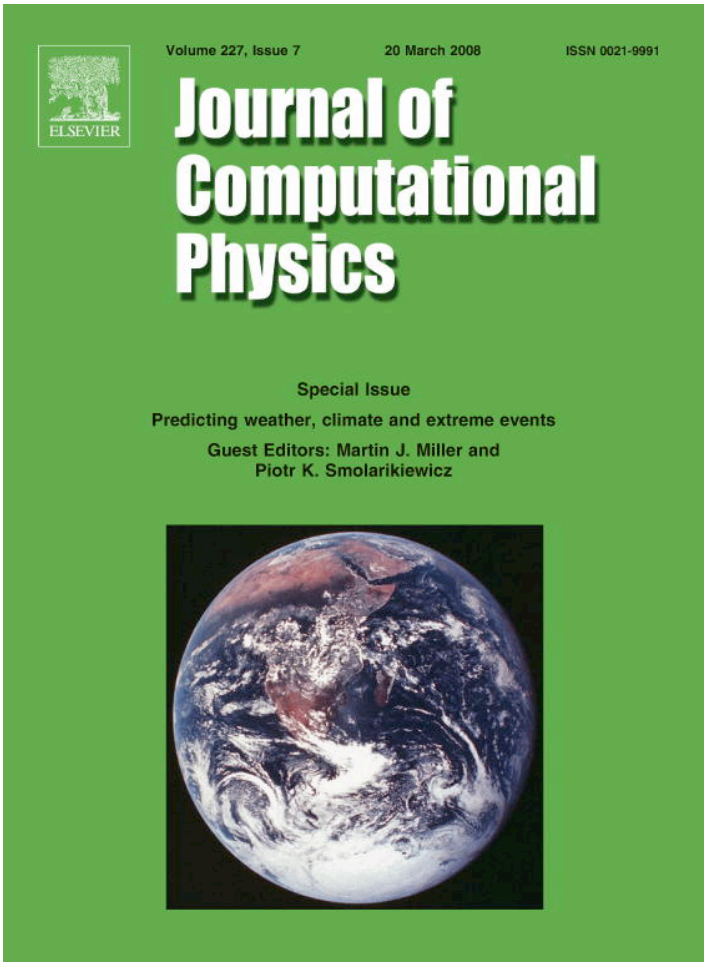

This article was published in an Elsevier journal. The attached copy is furnished to the author for non-commercial research and education use, including for instruction at the author's institution, sharing with colleagues and providing to institution administration.

Other uses, including reproduction and distribution, or selling or licensing copies, or posting to personal, institutional or third party websites are prohibited.

In most cases authors are permitted to post their version of the article (e.g. in Word or Tex form) to their personal website or institutional repository. Authors requiring further information regarding Elsevier's archiving and manuscript policies are encouraged to visit:

http://www.elsevier.com/copyright

Author's personal copy

Available online at www.sciencedirect.com
ScienceDirect
Journal of Computational Physics 227 (2008) 3465–3485
JOURNAL OF COMPUTATIONAL PHYSICS
www.elsevier.com/locate/jcp

A time-split nonhydrostatic atmospheric model for weather research and forecasting applications

William C. Skamarock *, Joseph B. Klemp

National Center for Atmospheric Research,[1] P.O. Box 3000, Boulder, CO, 80307-3000, USA

Received 6 July 2006; received in revised form 24 January 2007; accepted 25 January 2007
Available online 17 February 2007

Abstract

The sub-grid-scale parameterization of clouds is one of the weakest aspects of weather and climate modeling today, and the explicit simulation of clouds will be one of the next major achievements in numerical weather prediction. Research cloud models have been in development over the last 45 years and they continue to be an important tool for investigating clouds, cloud-systems, and other small-scale atmospheric dynamics. The latest generation are now being used for weather prediction. The Advanced Research WRF (ARW) model, representative of this generation and of a class of models using explicit time-splitting integration techniques to efficiently integrate the Euler equations, is described in this paper. It is the first fully compressible conservative-form nonhydrostatic atmospheric model suitable for both research and weather prediction applications. Results are presented demonstrating its ability to resolve strongly nonlinear small-scale phenomena, clouds, and cloud systems. Kinetic energy spectra and other statistics show that the model is simulating small scales in numerical weather prediction applications, while necessarily removing energy at the gridscale but minimizing artificial dissipation at the resolved scales. Filtering requirements for atmospheric models and filters used in the ARW model are discussed.
© 2007 Elsevier Inc. All rights reserved.

MCS: 65M06; 65M12; 76E06; 76R10; 76U05; 86A10

Keywords: Numerical methods; Time splitting; Numerical weather prediction; Compressible flow

1. Introduction

Efforts to simulate small-scale atmospheric flows where nonhydrostatic effects are important, such as eddies in the atmospheric boundary layer (ABL) having length scales of order a few kilometers or less, and deep convective clouds that can span the depth of the troposphere, are coincident with both the development of computational fluid dynamics and the evolution of computer technology. In the early 1960s, Lilly [22] performed simulations of ABL vortices and convective clouds using a time- and space-centered (leapfrog) integration

[1] The National Center for Atmospheric Research is sponsored by the National Science Foundation, Boulder, Colorado, USA.

* Corresponding author. Tel.: +1 303 497 8161.
E-mail address: skamaroc@ucar.edu (W.C. Skamarock).

0021-9991/$ - see front matter © 2007 Elsevier Inc. All rights reserved.
doi:10.1016/j.jcp.2007.01.037

Author's personal copy

scheme for the fully compressible 2D Euler equations. From that time to the present day, atmospheric modelers simulating small-scale motions have confronted a similar set of issues that can be categorized in two general (and overlapping) areas – how to formulate efficient solvers for small-scale nonhydrostatic low-Mach-number stratified flow, and how to model energy dissipation within these solvers. The lessons learned in these 40+ years of development have increasingly important applications outside the ongoing research simulation needs because these advances are now being brought to bear in operational numerical weather prediction. Presently, numerical simulations used to produce operational weather forecasts are being run with horizontal grid-spacings of a few kilometers and they are beginning to explicitly represent small-scale (nonhydrostatic) motions such as convective clouds.

We describe the formulation of a version of the Weather Research and Forecasting (WRF) Model called the Advanced Research WRF (ARW) in this paper. The ARW model represents the latest developments following a particular modeling approach that uses time-splitting techniques to efficiently integrate the fully compressible nonhydrostatic equations of motion. While the general approach described here was developed originally for cloud models [19], it is applicable to larger scales and has been used in a number of nonhydrostatic numerical weather prediction (NWP) models (e.g. MM5 [10], LM [8], COAMPS [14], ARPS [45]). We begin in Section 2.1 by briefly outlining the most popular approaches to designing nonhydrostatic atmospheric flow solvers, followed by a description of the ARW solver's continuous equations (Section 2.2), temporal discretization (Section 2.3) and spatial discretization (Section 2.4).

Atmospheric flow solutions do not converge in a strict sense; the model grid spacing is $\Delta x \sim$ O(km) but the Kolmogorov scale is $\sim$ O(cm), hence finer structures always appear with increasing resolution. Resolving these small structures is often the primary reason for increasing spatial resolution, thus an important aspect of a solver is its ability to correctly represent structures at the resolution limits (approximately $6\Delta x$–$10\Delta x$ for grid-point models). Hence in designing atmospheric models we seek to maintain accuracy and minimize artificial dissipation at the resolved scales while removing energy at the gridscale. In Section 3.1 we present results from the ARW model using idealized flow test cases, for which converged solutions exist, and we examine solver performance as the resolution is decreased and the main structures are only marginally resolved. Following this, simulations of observed severe weather events (Section 3.2) demonstrate the ability of the ARW model to capture important NWP phenomena, in this case tornadic thunderstorms and 2005 Hurricane Katrina. In Section 3.3 we examine some statistics of high-resolution ARW NWP forecasts demonstrating the energetics of the model, the changing dynamical nature of atmospheric flow from synoptic scales to cloud scales, and model filter performance. Section 3.4 contains a further discussion of model filtering. A summary is presented in Section 4.

2. ARW model formulation

2.1. Modeling approaches

Atmospheric flow solvers produce spatial and temporal integrations of the Euler equations, and accurate solutions for time-evolving flows (as opposed to steady state solutions) are of utmost importance for NWP and most research applications. The modes of meteorological interest in the Euler equation solutions are relatively slow – they rarely exceed Mach numbers of approximately 1/3 (for example, in the jet stream). The fast modes in the solutions are the acoustic modes and they contain no significant energy or amplitude relative to the meteorological modes of interest. Unfortunately, the acoustic modes present a significant timestep restriction in explicit time-integration methods.

Over the last 30 years three approaches have been used to circumvent the acoustic-mode timestep restriction. One class of approaches directly filters the acoustic modes from the continuous equations, and they are generically referred to as *anelastic* approximations. The first anelastic equation set was introduced by Ogura and Phillips [28]. This class of approximations is discussed in detail in [11] and references therein. These approaches work well in some flow regimes but may introduce errors in others [6]. Computationally, the approximations result in the need to solve a 3D Poisson equation each timestep. A second approach to circumvent the acoustic-mode restriction is to treat the acoustic modes implicitly in the time integration. These solvers, called *semi-implicit*, treat the time integration of the non-acoustic modes in an explicit manner and,

Author's personal copy

when combined with the implicit treatment of the acoustic modes, require the solution of a 3D Helmholtz equation each timestep. The method was first used in a cloud model by Tapp and White [40]. To further relax the integration timestep constraint, the semi-implicit treatment of acoustic and gravity wave modes has been combined with a Lagrangian treatment of advection during each timestep. The semi-Lagrangian formulation adds significant computational expense that is typically offset by using a large timestep (where Courant numbers are significantly greater than unity). The need to solve a multidimensional Helmholtz problem each timestep is a drawback of the method, and the methods are usually only stable in first order time-integration schemes (the Crank–Nicholson centered implicit discretization of the acoustic terms is often forward weighted to stabilize the full time-integration scheme). Examples of a model of this type are the semi-implicit semi-Lagrangian model (e.g. [3,38]). These approaches have proven very effective in global models, where the converging longitude lines at the poles would impose severe restrictions on timesteps used in an explicit model with a latitude-longitude grid. For cloud and mesoscale applications, however, time steps required to properly represent important features are typically comparable to those used in explicit time integration schemes [2].

Given the drawbacks of filtering acoustic modes from the continuous equations and in constructing solvers using semi-implicit formulations, we have chosen to use time-splitting methods to efficiently solve the full Euler equations. The time-splitting methods involve integrating terms associated with the acoustic modes with smaller timesteps than those associated with the meteorologically significant (low frequency) modes. The methods maintain much of the simplicity of fully-explicit solvers and have proven more efficient than semi-implicit methods for limited-area NWP applications (i.e. maximum Mach numbers $\sim 1/3$; [41]) although semi-implicit methods may be more efficient for very low Mach number flows found in some research applications. High-order time and space discretizations can also be easily implemented within the splitting methods. Being explicit, the solvers are Courant-number limited, hence they have found their greatest use in limited area NWP (where only a portion of the globe is covered with a grid that is relatively isotropic) where the pole problems associated with the latitude-longitude discretization do not exist.

2.2. Continuous equations

2.2.1. Euler equations using a hydrostatic pressure vertical coordinate

The continuous equations solved in the ARW model are the Euler equations cast in a flux (conservative) form where the vertical coordinate, denoted as η, is defined by a normalized hydrostatic pressure (or mass) following Laprise [20]:

$$\eta = (p_{\mathrm{h}} - p_{\mathrm{ht}})/\mu \quad \text{where } \mu = p_{\mathrm{hs}} - p_{\mathrm{ht}}, \tag{1}$$

where p_{h} is the hydrostatic component of the pressure, and p_{hs} and p_{ht} are the values for the dry atmosphere at the surface and top boundaries, respectively. Following common practice, we set $p_{\mathrm{ht}} = \text{constant}$. η decreases monotonically from a value of 1 at the surface to 0 at the upper boundary of the model domain. This coordinate definition proposed by Laprise, and depicted in Fig. 1, is the traditional σ coordinate used in many hydrostatic atmospheric models.

Using this vertical coordinate, the flux form equations are expressed as:

$$U_t + (\nabla \cdot \mathbf{V}u) + \mathrm{P}_x(p,\phi) = F_U, \tag{2}$$
$$V_t + (\nabla \cdot \mathbf{V}v) + \mathrm{P}_y(p,\phi) = F_V, \tag{3}$$
$$W_t + (\nabla \cdot \mathbf{V}w) + \mathrm{P}_\eta(p,\mu) = F_W, \tag{4}$$
$$\Theta_t + (\nabla \cdot \mathbf{V}\theta) = F_\Theta, \tag{5}$$
$$\mu_t + (\nabla \cdot \mathbf{V}) = 0, \tag{6}$$
$$\phi_t + \mu^{-1}[(\mathbf{V} \cdot \nabla\phi) - gW] = 0, \tag{7}$$
$$(Q_m)_t + (\nabla \cdot \mathbf{V}Q_m) = F_{Q_m}, \tag{8}$$

where $\mu(x,y)$ represents the mass of the dry air per unit area within the column in the model domain at (x,y), hence the flux form variables are defined as

Author's personal copy

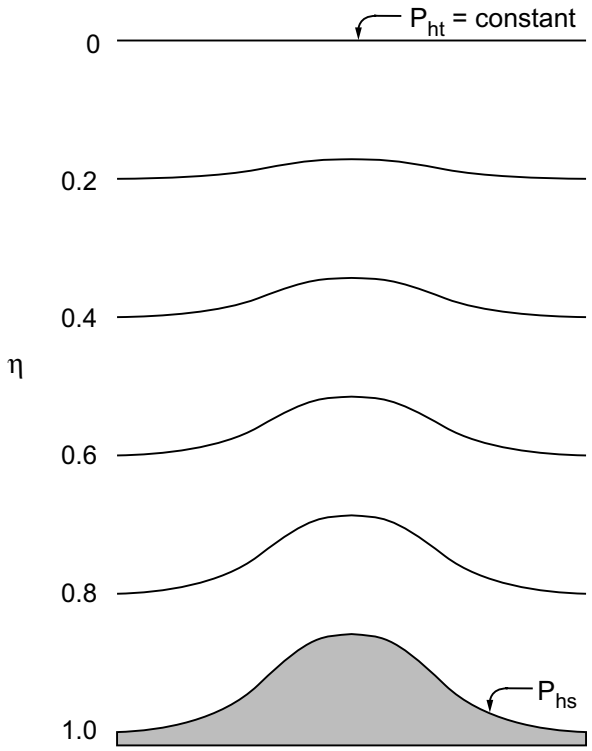

Fig. 1. Schematic of the terrain following σ coordinate.

$$U = \mu u/m, \quad V = \mu v/m, \quad W = \mu w/m, \quad \Omega = \mu\dot{\eta}/m,$$

where m is a map-scale factor that allows mapping of the equations to the sphere (see [13]) and is given as

$$m = \frac{(\Delta x, \Delta y)}{\text{distance on the earth}}.$$

The velocities $\mathbf{v} = (u, v, w)$ are the physical velocities in the two horizontal and vertical directions, respectively, $\omega = \dot{\eta}$ is the transformed 'vertical' velocity, and θ is the potential temperature. $Q_m = \mu q_m$; $Q_m = Q_v, Q_c, Q_i, \ldots$, represent the mass of water vapor, cloud, rain, ice, etc., and q_* are their mixing ratios (mass per mass of dry air). We also define non-conserved variables $\phi = gz$ (the geopotential), p (pressure), and $\alpha = 1/\rho$ (the specific volume) that appear in the governing equations. α_d refers to the specific volume of the dry air, and α is the specific volume including all moist species, i.e. $\alpha = \alpha_d(1 + q_v + q_c + q_i \cdots)^{-1}$.

To close the system, we use the diagnostic relation for the specific volume (that is, the hydrostatic relation for dry air)

$$\phi_\eta = -\alpha_d \mu, \tag{9}$$

and the moist equation of state

$$p = p_0(R_d\theta(1 + (R_d/R_v)q_v)/p_0\alpha_d)^\gamma, \tag{10}$$

where $\gamma = c_p/c_v = 1.4$ is the ratio of the heat capacities for dry air, R_d is the gas constant for dry air, and p_0 is a reference pressure (typically 10^5 Pa).

In this paper x, y, η and t subscripts denote partial differentiation, and

$$\nabla \cdot \mathbf{V}a = m^2[(Ua)_x + (Va)_y] + (\Omega a)_\eta,$$
$$\mathbf{V} \cdot \nabla a = m^2[Ua_x + Va_y] + m\Omega a_\eta,$$

where a represents a generic scalar variable. The pressure gradient terms in (2)–(4) are given by

Author's personal copy

$$\mathrm{P}_x(p,\phi) = (\alpha/\alpha_\mathrm{d})[-\partial_x(p\phi_\eta) + \partial_\eta(p\phi_x)]|,$$
$$\mathrm{P}_y(p,\phi) = (\alpha/\alpha_\mathrm{d})[-\partial_y(p\phi_\eta) + \partial_\eta(p\phi_y)],$$
$$\mathrm{P}_\eta(p,\mu) = -gm^{-1}[(\alpha/\alpha_\mathrm{d})p_\eta - \mu].$$

The right-hand-side (RHS) terms F_U, F_V, F_W, F_Θ and F_{Q_m} represent forcing terms arising from model physics, turbulent mixing, spherical projections, the earth's rotation, and moist physics and are described in detail in [33].

We have chosen to use a conservation equation for the dry air (6) so that no source terms appears in it. All the prognostic Eqs. (2)–(8) are cast in conservative form except for (7) which is the material derivative of the definition of the geopotential. This equation could be cast in flux form but we find no advantage in doing so since $\mu\phi$ is not a conserved quantity. We could also use a prognostic pressure equation in place of (7) [20], but pressure is not a conserved variable and we could not use a prognostic pressure equation together with the conservation equation for Θ (5) because they are linearly dependent. Additionally, prognostic pressure equations have the disadvantage of possessing a mass divergence term multiplied by a large coefficient (proportional to the square of the sound speed) that makes spatial and temporal discretization problematic. It should be noted that the relation for the hydrostatic balance (9) does not represent a constraint on the solution, rather it is a diagnostic relation that formally is part of the coordinate definition. In the hydrostatic counterpart to the nonhydrostatic equations, the vertical momentum equation (4) is replaced by $(\alpha/\alpha_\mathrm{d})p_\eta = \mu$.

2.2.2. Perturbation formulation

The earth's atmosphere is strongly stratified and it is in approximate hydrostatic balance. In order to reduce truncation errors in the horizontal pressure gradient calculations in the discrete solver, in addition to reducing machine rounding errors in the vertical pressure gradient and buoyancy calculations, we recast the thermodynamic variables into a reference profile plus a perturbation: $p = \bar{p}(\bar{z}) + p'$, $\phi = \bar{\phi}(\bar{z}) + \phi' = g\bar{z} + gz'$, $\alpha = \bar{\alpha}(\bar{z}) + \alpha'$, and $\mu = \bar{\mu}(x,y) + \mu'$. The reference profile is in hydrostatic balance. Because the η coordinate surfaces are generally not horizontal, the reference profiles $\bar{p}$, $\bar{\phi}$, and $\bar{\alpha}$ are functions of (x,y,η). At the model top ($\eta = 0$), $p(x,y,0) = p_\mathrm{ht} = \bar{p}(\bar{z})$, and $p'(x,y,0) = 0$. With the introduction of the perturbation variables, the pressure gradient operators are redefined as

$$\begin{aligned}
\mathrm{P}_x(p',\alpha',\phi',\mu') &= (\mu\alpha p'_x + \mu\alpha'\bar{p}_x) + (\alpha/\alpha_\mathrm{d})(\mu\phi'_x + p'_\eta\phi_x - \mu'\phi_x),\\
\mathrm{P}_y(p',\alpha',\phi',\mu') &= (\mu\alpha p'_y + \mu\alpha'\bar{p}_y) + (\alpha/\alpha_\mathrm{d})(\mu\phi'_y + p'_\eta\phi_y - \mu'\phi_y),\\
\mathrm{P}_\eta(p',\mu') &= -m^{-1}g(\alpha/\alpha_\mathrm{d})[p'_\eta - \bar{\mu}_\mathrm{d}(q_v + q_c + q_r)] + m^{-1}\mu' g,
\end{aligned} \tag{11}$$

and the hydrostatic relation for dry air (9) becomes

$$\phi'_\eta = -\bar{\mu}\alpha'_\mathrm{d} - \alpha_\mathrm{d}\mu'_\mathrm{d}. \tag{12}$$

Eqs. (2)–(8), using the perturbation formulation (11) and (12), form the basis for the discrete solver.

2.3. Temporal discretization

2.3.1. Overview of the Runge–Kutta time integration

Most time-split nonhydrostatic NWP models (e.g. ARPS, COAMPS, MM5, LM) use a leapfrog time discretization for the slow modes, and dissipation terms are commonly integrated forward in time (see [35]). Many semi-implicit models also use leapfrog time integration for the explicit (slow-mode) terms, although a number of these have switched to forward-in-time integration schemes. In the ARW model, we use an original third-order Runge–Kutta type scheme (RK3) developed in [44] as the basis for the time-split scheme. The RK3 scheme is not a standard Runge–Kutta scheme per se because, while it is third-order accurate for linear equations, it is only second-order accurate for nonlinear equations [31]. The scheme is, however, more easily adaptable for stable time-splitting than other Runge–Kutta variants we have examined.

The RK3 scheme circumvents three problems inherent in the leapfrog scheme. First, while the leapfrog scheme is second-order accurate, the scheme requires temporal filtering to prevent decoupling of the timesteps

Author's personal copy

which reduces the accuracy to first order. The RK3 scheme does not require this filtering. Second, the leapfrog scheme possesses large phase errors compared to the RK3 scheme. Third, the RK3 scheme allows both neutral and dissipative (upwind-biased) spatial discretizations for advection, whereas leapfrog is stable only for centered (neutral) operators [35].

Defining the prognostic variables in the ARW solver as $(\Phi = (U, V, W, \Theta, \phi', \mu', Q_m))$ and the model equations as $\Phi_t = R(\Phi)$, the RK3 integration takes the form of three steps to advance a solution $\Phi(t)$ to $\Phi(t + \Delta t)$:

$$\Phi^* = \Phi^t + \frac{\Delta t}{3} R(\Phi^t), \tag{13}$$

$$\Phi^{**} = \Phi^t + \frac{\Delta t}{2} R(\Phi^*), \tag{14}$$

$$\Phi^{t+\Delta t} = \Phi^t + \Delta t R(\Phi^{**}), \tag{15}$$

where Δt is the time step for the low-frequency modes (the model time step), and superscripts denote time levels. With respect to the ARW equations, the time derivatives Φ_t are the partial time derivatives (the left-most terms) in Eqs. (2)–(8), and $R(\Phi)$ are the right-hand side terms in (2)–(8) in addition to the advection terms.

2.3.2. Time-split acoustic-mode integration

The high-frequency acoustic modes are meteorologically insignificant [28] and would severely limit an explicit RK3 time step Δt. To circumvent this time step limitation we use a time-split version of the RK3 scheme [44]. The time-splitting technique involves integrating terms associated with acoustic modes with smaller time-steps than the low-frequency (meteorologically significant) modes. Within the small timestep integration, terms associated with horizontally propagating modes are integrated explicitly, while terms associated with vertically propagating modes are integrated implicitly. The implicit integration component alleviates the severe Courant number restriction, arising from vertically propagating acoustic modes when using grids with large aspect ratios $\Delta x/\Delta z$, at the cost of a simple tridiagonal matrix inversion.

We integrate a perturbation form of the governing equations on the smaller acoustic time steps within the RK3 large-time-step sequence in order to increase the accuracy of the splitting [17]. To form the perturbation equations, we follow [17] and define small time step variables that are deviations from the most recent RK3 predictor (denoted by the superscript t^*) and representing either Φ^t, Φ^*, or Φ^{**} in (13)–(15):

$$\mathbf{V}'' = \mathbf{V} - \mathbf{V}^{t^*}, \quad \Omega'' = \Omega - \Omega^{t^*}, \quad \Theta'' = \Theta - \Theta^{t^*},$$
$$\phi'' = \phi' - \phi'^{t^*}, \quad \alpha_d'' = \alpha_d' - \alpha_d'^{t^*}, \quad \mu'' = \mu' - \mu'^{t^*}.$$

The hydrostatic relation (i.e., the vertical coordinate definition) becomes

$$\alpha_d'' = -\frac{1}{\mu^{t^*}} \left(\phi_\eta'' + \alpha_d^{t^*} \mu'' \right). \tag{16}$$

To achieve a linear implicit system for the vertically propagating acoustic modes, we introduce a version of the equation of state that is linearized about t^*:

$$p'' = \frac{c_s^2}{\alpha_d^{t^*}} \left(\frac{\Theta''}{\Theta^{t^*}} - \frac{\alpha_d''}{\alpha_d^{t^*}} - \frac{\mu''}{\mu^{t^*}} \right), \tag{17}$$

where $c_s^2 = \gamma p^{t^*} \alpha_d^{t^*}$ is the square of the sound speed. By combining (16) and (17), the vertical pressure gradient can be expressed as:

$$p_\eta'' = (C \phi_\eta'')_\eta + \left(\frac{c_s^2}{\alpha_d^{t^*}} \frac{\Theta''}{\Theta^{t^*}} \right)_\eta, \tag{18}$$

where $C = c_s^2/\mu^{t^*} \alpha^{t^* 2}$. Given the time-scales of the meteorological modes, this linearization is sufficient to maintain the overall accuracy of the solver.

The perturbation variables, along with (18), are substituted into the prognostic equations and lead to the acoustic time-step equations:

Author's personal copy

$$\delta_\tau U'' + \mathrm{P}_x(p'', \alpha'', \phi'', \mu'')^\tau = -\nabla\cdot(\mathbf{V}u)^{t^*} - \mathrm{P}_x(p', \alpha', \phi', \mu')^{t^*} + F_U, \tag{19}$$

$$\delta_\tau V'' + \mathrm{P}_y(p'', \alpha'', \phi'', \mu'')^\tau = -\nabla\cdot(\mathbf{V}v)^{t^*} - \mathrm{P}_y(p', \alpha', \phi', \mu')^{t^*} + F_V, \tag{20}$$

$$\delta_\tau \mu'' + \nabla\cdot\mathbf{V}''^{\tau+\Delta\tau} = -\nabla\cdot\mathbf{V}^{t^*}, \tag{21}$$

$$\delta_\tau \Theta'' + \nabla\cdot(\mathbf{V}^{\tau+\Delta\tau}\theta^{t^*}) = -\nabla\cdot(\mathbf{V}\theta)^{t^*} + F_\Theta, \tag{22}$$

$$\delta_\tau W'' + \overline{\mathrm{P}''_\eta(\phi'', \Theta'', \mu'')^\tau} = -\nabla\cdot(\mathbf{V}w)^{t^*} - \mathrm{P}_\eta(p', \mu')^{t^*} + F_W, \tag{23}$$

$$\delta_\tau \phi'' + \frac{1}{\mu^{t^*}}\left[m\Omega''^{\tau+\Delta\tau}\phi_\eta - \overline{gW''}^\tau\right] = -\mu^{-1}[\mathbf{V}\cdot\nabla\phi - gW]^{t^*}, \tag{24}$$

where

$$\mathrm{P}''_\eta(\phi'', \Theta'', \mu'') = -m^{-1}g\left[(\alpha/\alpha_\mathrm{d})^{t^*}\left[(C\phi''_\eta)_\eta + \left(\frac{c_\mathrm{s}^2}{\alpha^{t^*}}\frac{\Theta''}{\Theta^{t^*}}\right)_\eta\right] - \mu''\right].$$

The RHS terms in (19)–(24) are fixed for the acoustic steps that comprise the time integration of each RK3 sub-step (13)–(15). The acoustic step equations utilize the discrete acoustic time-step operator defined as

$$\delta_\tau a = \frac{a^{\tau+\Delta\tau} - a^\tau}{\Delta\tau},$$

where $\Delta\tau$ is the acoustic time step, and an acoustic time-step averaging operator is defined as

$$\bar{a}^\tau = \frac{1+\beta}{2}a^{\tau+\Delta\tau} + \frac{1-\beta}{2}a^\tau,$$

where β is a user-specified off-centering parameter. Eqs. (23) and (24), with the time-averaged terms, comprise the vertically implicit acoustic mode integration. The off-centering parameter β will forward center the time average as is the common approach in 3D semi-implicit nonhydrostatic models. Here, the off-centering is applied over smaller acoustic timesteps and does not degrade the formal accuracy of the solver.

The integration over the acoustic time steps proceeds as follows. Beginning with the small time-step variables at time τ, (19) and (20) are stepped forward to obtain $U''^{\tau+\Delta\tau}$ and $V''^{\tau+\Delta\tau}$. Both $\mu''^{\tau+\Delta\tau}$ and $\Omega''^{\tau+\Delta\tau}$ are then calculated by advancing (21). This is accomplished by first integrating (20) vertically from the surface to the material surface at the top of the domain, which removes the $\partial_\eta\Omega''$ term such that

$$\delta_\tau \mu'' = m^2\int_1^0 \left[(U'' + U^{t^*})_x + (V'' + V^{t^*})_y\right]^{\tau+\Delta\tau} \mathrm{d}\eta.$$

After computing $\mu''^{\tau+\Delta\tau}$, $\Omega''^{\tau+\Delta\tau}$ is recovered by vertically integrating (21) to recover Ω''. Eq. (22) is then stepped forward to calculate $\Theta''^{\tau+\Delta\tau}$. The forward integration of the horizontal momentum equations (19) and (20), followed by the backward integration of the continuity equation (21) and the thermodynamic equation (22), constitute the explicit forward–backward integration scheme of Mesinger [25]. Following this explicit integration, (23) and (24) are combined to form a vertically implicit equation that is solved for $W''^{\tau+\Delta\tau}$ subject to the boundary conditions $W'' = \mathbf{V}''\cdot\nabla h$ at the lower boundary $z = h(x, y)$ and $p' = 0$ along the model top. $\phi''^{\tau+\Delta\tau}$ is then obtained from (24) and $p''^{\tau+\Delta\tau}$ and $\alpha_\mathrm{d}''^{\tau+\Delta\tau}$ are recovered from (16) and (17).

The acoustic-integration equations (19)–(24) and the integration sequence just described represent a specific splitting of the equations and LHS terms. The splitting is not arbitrary, it is derived from a careful examination of the dispersion relation for the acoustic and gravity waves as described in [17]. Additionally, the small-timestep acoustic integration incorporates the gravity wave terms. The gravest gravity-wave mode is the external mode which propagates at speeds similar to the acoustic modes, hence handling these modes on the acoustic step is necessary [17].

2.3.3. Full time-split integration scheme

The RK3 time-step integration sequence, including the acoustic substeps, is depicted in Fig. 2. In the integration n represents the number of acoustic time steps for a given substep of the RK3 integration and n_s is the ratio of the RK3 time step to the acoustic time step for the second and third RK3 substeps. Model physics

Author's personal copy

Begin Time Step
Begin RK3 Loop: Steps 1, 2, and 3
(1) If RK3 step 1, compute and store F_Φ
(i.e., physics tendencies for RK3 step, including mixing).
(2) Compute RHS of (19)-(24).
Begin Acoustic Step Loop: Steps $1 \rightarrow n$,
RK3 step 1, $n = 1, \quad \Delta\tau = \Delta t/3;$
RK3 step 2, $n = n_s/2, \ \Delta\tau = \Delta t/n_s;$
RK3 step 3, $n = n_s, \quad \Delta\tau = \Delta t/n_s.$
(3) Advance horizontal momentum using (19) and (20).
(4) Advance μ (21), compute $\Omega''^{\tau+\Delta\tau}$,
then advance Θ using (22).
(5) Advance W and ϕ (23) and (24).
(6) Diagnose p'' and α'' using (16) and (17).
End Acoustic Step Loop
(7) Advance scalars over the RK3 substep
using mass fluxes U, V and Ω
time-averaged over the acoustic steps.
(8) Compute α' and p' using (12) and (10)
and the updated prognostic variables.
End RK3 Loop
(9) Compute non-RK3 physics (currently microphysics)
and advance variables.
End Time Step

Fig. 2. The time-split ARW integration sequence.

(processes not contained within the Euler equations) and sub-grid processes (e.g. turbulence that is part of the Euler equation solutions but is not resolved on a given grid) are integrated within the RK3 time integration (using a forward time step, i.e., step (1)) or the RK3 time integration if higher temporal accuracy is desired, i.e., in step (2) – implying a physics evaluation every RK3 substep, or external to it using additive time-splitting, i.e., step (9). Note that within the first RK3 substep, a single acoustic time step is used to advance the solution regardless of n_s. Within the full RK3-acoustic time-split integration, this modified acoustic time step does not impose any additional stability constraints [44].

The major costs in the model arise from the evaluation of the right-hand side terms in (19)–(24). The efficiency of the RK3 time-split scheme arises from the fact that the RK3 time step Δt is much larger than the acoustic time step $\Delta\tau$, hence the most costly evaluations are only performed in the less-frequent RK3 steps.

2.4. Spatial discretization

2.4.1. Grid structure and basic spatial discretization

The spatial discretization for the ARW model is performed on a staggered C-grid as shown in Fig. 3. This staggering is used in most nonhydrostatic NWP and research models (e.g. ARPS [45], COAMPS [14], RAMS [30], LM [8], GEM [46], MC2 [3], UKMO Unified Model [38], JMA Nonhydrostatic model [32]) because it provides the most accurate representation of gravity waves (horizontally divergent modes [26]). Unstaggered grids are also used in nonhydrostatic models. An unstaggered grid admits the possibility of null modes in the solution (e.g. the decoupling of the odd and even gridpoint pressure values). However, it is used in some models because it simplifies semi-Lagrangian formulations [39] by allowing for a single advective formulation for

Author's personal copy

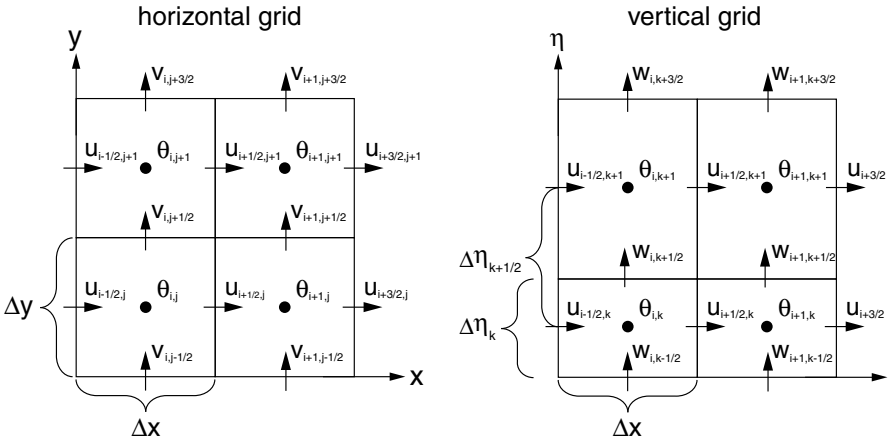

Fig. 3. Horizontal (left) and vertical (right) staggering for the C-grid.

all variables. Other staggerings are used in hydrostatic large-scale models that provide for higher accuracy in the rotational modes [26]. In nonhydrostatic model applications the Rossby numbers are large for the small scales and increased accuracy for the rotational modes is not needed. The C-grid staggering allows for a discretization of the pressure gradient and divergence terms across a single grid interval without any averaging, achieving a highly accurate second-order difference. The timestep constraint associated with a one-grid-interval gradient operator is relaxed by a factor of 2 with the use of the explicit forward–backward acoustic-mode integration outlined in the previous section.

2.4.2. Advection (flux divergence) discretization

While the spatial discretization of the pressure gradient and divergence terms is second order and centered, the advection (flux divergence) terms are discretized using selectable second through sixth-order operators as given in [15] (we comment on the rational for the mixed approximation in the next section). The discrete flux divergence operators can be illustrated by considering the flux divergence operator for a scalar q in its discrete form:

$$\nabla \cdot \mathbf{V}a = m^2[\delta_x(U\bar{q}^{x_{\mathrm{adv}}}) + \delta_y(V\bar{q}^{y_{\mathrm{adv}}})] + m\delta_\eta(\Omega\bar{q}^{\eta_{\mathrm{adv}}}).$$

The discrete operator δ_x is defined as

$$\delta_x(U\bar{q}^{x_{\mathrm{adv}}}) = \Delta x^{-1}[(U\bar{q}^{x_{\mathrm{adv}}})_{i+1/2} - (U\bar{q}^{x_{\mathrm{adv}}})_{i-1/2}].$$

The different order advection schemes correspond to different definitions for the operator $\bar{q}^{x_{\mathrm{adv}}}$. For illustrative purposes, the sixth and fifth-order operators are

$$\text{sixth order}: \quad (\bar{q}^{x_{\mathrm{adv}}})_{i-1/2} = \frac{37}{60}(q_i + q_{i-1}) - \frac{2}{15}(q_{i+1} + q_{i-2}) + \frac{1}{60}(q_{i+2} + q_{i-3}),$$

$$\text{fifth order}: \quad (\bar{q}^{x_{\mathrm{adv}}})_{i-1/2} = (\bar{q}^{x_{\mathrm{adv}}})^{6^{\mathrm{th}}}_{i-1/2} - \mathrm{sign}(U)\frac{1}{60}[(q_{i+2} - q_{i-3}) - 5(q_{i+1} - q_{i-2}) + 10(q_i - q_{i-1})],$$

where the scalar q in these operators correspond to the latest predictors (Φ', Φ^* or Φ^{**}) in the RK3 scheme (13)–(15). The even-order advection operators are spatially centered and thus contain no implicit diffusion outside of the damping inherent in the RK3 time integration. The odd-order operators are upwind-biased, and the spatial discretization is inherently diffusive. As is evident in the formulation, the odd-order operators are comprised of the next higher (even) order centered operator plus an upwind term that, for a constant transport mass flux, is a diffusion term of the next higher (even) order with a hyper-viscosity proportional to the Courant number. Also in the RK3 implementation, the 3D time-dependent advection discretization is fully third order in both time and space even though the advection operators are applied along gridlines; the higher-order cross-derivative terms in the Taylor series expansion are picked up through the multiple RK3 substeps. The order of accuracy is, however, only formally third order for constant U; for non-constant velocities the scheme is only second-order accurate. Further details concerning RK3 advection can be found in [44,15].

Author's personal copy

3. Model performance

In designing solvers we wish to maximize solver efficiency, that is, maximize the solution accuracy for a given computational expense or minimize the computational expense for a required accuracy. This requires the ability to objectively measure solution accuracy for relevant applications of the solver, and a problem we encounter when testing models is that the model solutions for our applications do not converge – spatial grid refinement leads to the appearance of smaller-scale features in the flow. Indeed, the reason for increasing resolution in our applications is often to explicitly resolve these newly appearing smaller-scale features. This non-convergence is the result of the solvers' sub-grid models for turbulence and other parameterized physics not explicitly contained in the Euler equations. Thus, while higher-order convergence in a solver might be a desired feature in some fluid-flow solver applications, the ability of a solver to resolve fine-scale structure (relative to the mesh) is the most important aspect of solver performance in NWP and small-scale atmospheric simulations. In this regard it should be appreciated that the large-scale features are well-resolved with any reasonable discretization, even a low-order one.

The most efficient solvers we have been able to develop have used higher-order discretizations in selected parts of the solver design. Specifically, we have found that it is most advantageous to use a high-order transport (advection) scheme in the solver. Conversely, we have found that approximations higher than second-order for centered discretization over one grid interval in other parts of the solver (e.g., the pressure gradient terms) do not appreciably improve the representation of the small scales features in the solutions.

We are using a split-explicit time integration scheme, and we make selective use of high order approximations in transport and aspects of the time integration scheme because we believe they maximize efficiency and are robust. Other aspects of the solver design are influenced by our applications. We are using an equation set cast in conservative (flux) form because of our desire to numerically conserve first order quantities such as mass, entropy, and scalars (following Ooyama [29]) and because many applications require conserving solvers, such as air quality applications and atmospheric chemistry. Most existing cloud and mesoscale models do not exactly conserve anything, even mass (e.g., MM5, ARPS, COAMPS, LM, and most semi-Lagrangian semi-implicit formulations [39]), in part because it has not been obvious how to design efficient and robust conservative formulations. These models have performed adequately because conservation is not important in most applications for which they are used. We believe the use of conservative continuous and discrete equations, and the use of high-order temporal integration and advection (the RK3 scheme and high-order upwind-biased advection), represent the major advances in the ARW model from the preceding generation of models (MM5, ARPS, COAMPS, LM, etc.).

With these points in mind, the test results presented in this section are designed to illustrate the ability of the ARW model to resolve structures at the limit of its resolution capabilities, and to determine the resolution limits. Although there are no standard test suites for nonhydrostatic atmospheric models, a number of linear and fewer nonlinear analytic solutions, and some converged numerical solutions, have been used to evaluate their robustness and accuracy as fluid flow solvers. For example, there are a number of linear steady-state mountain-wave solutions describing stratified flow over some topographic feature (see [12] and references therein). However, for small-scale (nonhydrostatic) atmospheric flow and for high-resolution NWP, the flows of interest are highly nonlinear and transient, thus many standard tests have little relevance to research and NWP needs. Consider cloud simulations. Clouds represent strongly nonlinear, transient flow features that are discontinuous at the cloud/clear air interface. The modeling of deep convective clouds, and the interaction between these clouds and the larger-scale environment, is an active area of research and is producing results that will be used in operational NWP in the very-near future. We do not have any analytic solutions for these strongly nonlinear, transient flows.

3.1. Gravity current test case

The test case described in Straka et al. [37] for a nonlinear density current simulation has been widely used for nonhydrostatic model intercomparison. By employing a constant fixed eddy viscosity in a second-order mixing formulation, converged numerical solutions can be computed. The complete configuration for the

Author's personal copy

2D test case is described in Straka et al., where results for 14 different solvers are presented. Results for this test case from an early advective-form of the RK3 time-split model are presented in [44].

Fig. 4 is a plot of the potential temperature field from the ARW model that can be compared with the results shown in [12,44]. The results produced by the flux (conservative) form ARW model are similar to those produced by the advective form model presented in [44]. The models both show approximately third-order convergence for this problem and both show the greater accuracy of the high-order solver (third-order RK3 time integration and fifth-order advection) compared to lower order solvers (see also [44], and compare both with solutions from other models given in [37]).

The $\Delta x = 50$ m solution shown in the figure is essentially converged for this case, and the converged solution is very similar to other published solutions (the constant pressure upper boundary condition differs from the rigid lid upper boundary condition used in most of the other solutions leading to the small differences among the solutions – see [37] for further discussion of converged-solution differences). As expected, coarsening of the grid leads to a degradation of the solution. Significant dissipation produced by the fifth-order advection scheme is evident in the simulations depicted in the left column in the $\Delta x = 400$ m solution. The solutions produced using the second-order centered scheme, depicted in the right column of Fig. 4, show significant degradation of the solution even at $\Delta x = 100$ m (compare the $\Delta x = 50$ m and 100 m eddy structure), whereas the ARW solutions computed using the fifth-order advection scheme on the $\Delta x = 50$ m and 100 m are almost indistinguishable.

In order to examine phase errors, a constant horizontal wind is used in the initial state to translate the solution. Fig. 5 shows the second and fifth-order advection solutions using an initially uniform horizontal wind. Both the left and right moving gravity currents are shown in the plots and the solution should be symmetric about the translating centerline. Larger phase errors are evident in the solution computed using second-order advection on both 100 m and 200 m grids compared with the fifth-order advection on the 200 m grid.

The larger phase errors and associated lack of symmetry, and the obvious lower accuracy of the second-order advection scheme compared with the fifth-order scheme, has led us to adopt the higher order scheme in our ARW applications. Additionally, in these tests we have used the RK3 time-integration scheme; simu-

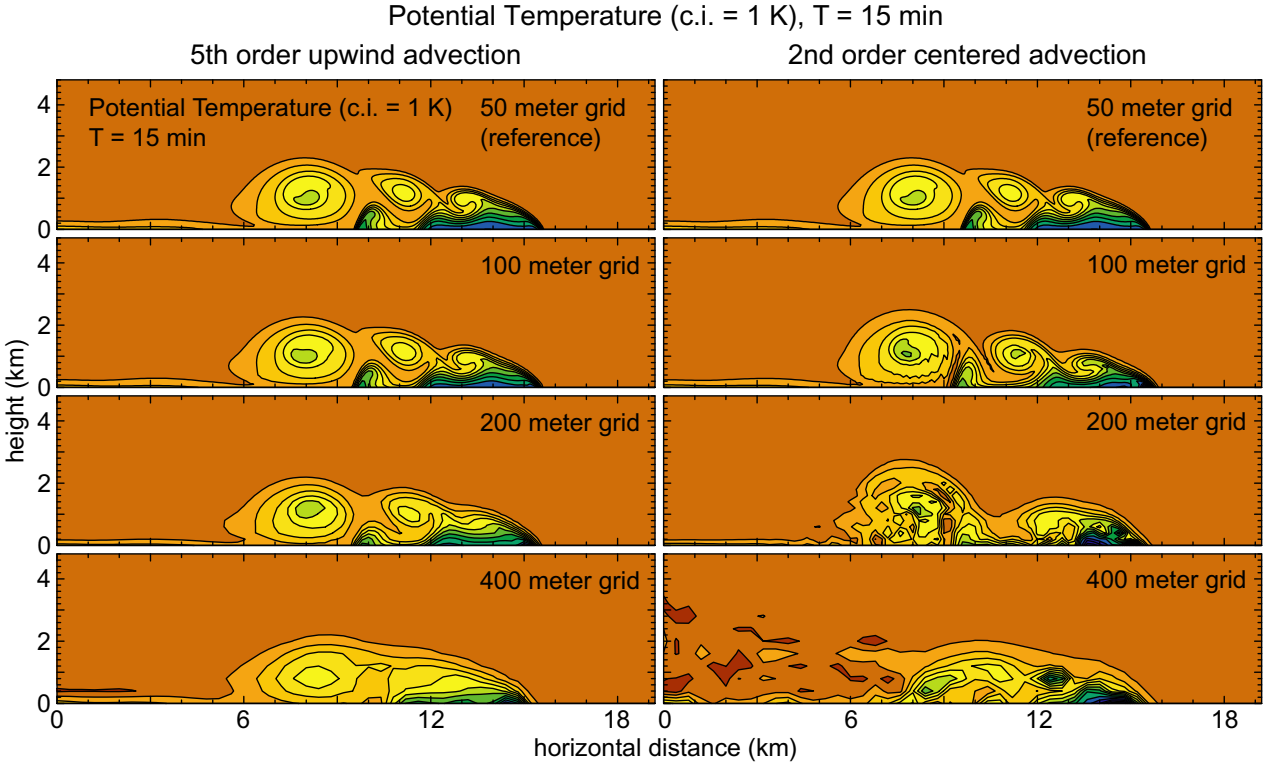

Fig. 4. Fifth-order and second-order advection operator solutions for the Straka [37] gravity current test case. The timesteps used in these simulations are 0.5, 1, 2 and 4 s on the 50, 100, 200 and 400 m grids, respectively.

Author's personal copy

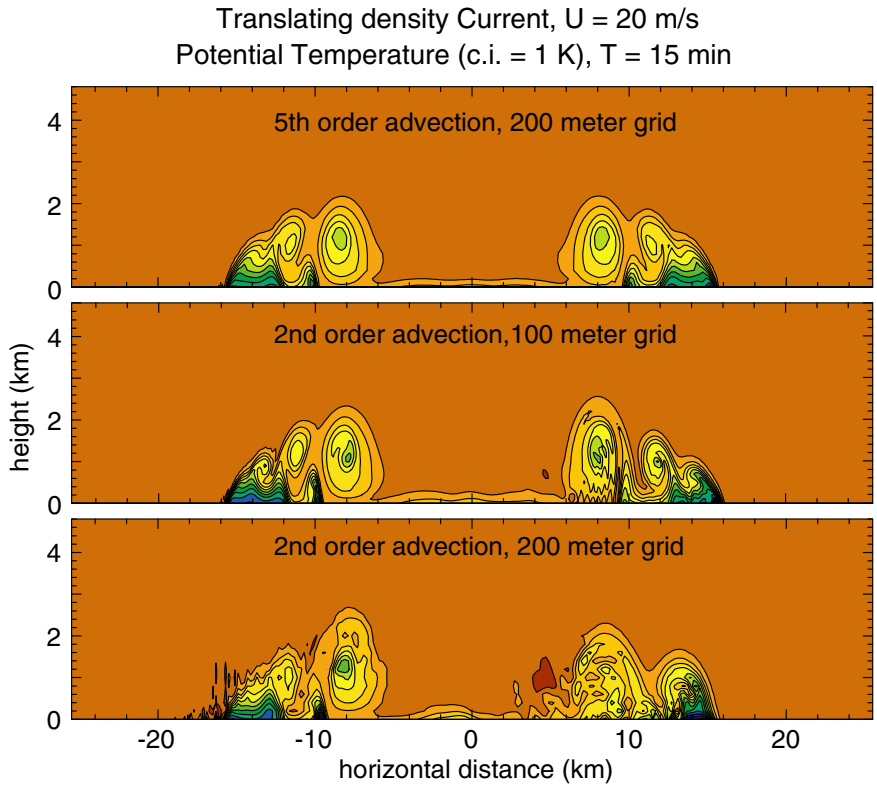

Fig. 5. Straka [37] test case with a translating solution using second- and fifth-order advection operators.

lations using leapfrog would exhibit increased phase errors. We have also experimented with higher-order approximations in other parts of the model, including the pressure gradient terms in the momentum equations and the mass divergence operator in the continuity equation. We have not found a significant improvement in solution accuracy using these higher order approximations for marginally resolved features such as the gravity current simulations we present here on the $\Delta x = 200$ m and 400 m grids.

3.2. NWP tests: convection-permitting simulations

Over the past several years, nonhydrostatic NWP models have been tested using grid spacings where deep unstable convection is explicitly simulated, that is, a parameterization of deep convective clouds and their effects (a sub-grid model of deep convection, typically referred to as a convective parameterization) is not used. Deep convection is a crucial component of many important atmospheric phenomena (hurricanes, mid-latitude squall-lines, tornadic storms, tropical cloud clusters, etc.) and an explicit representation of deep convective clouds includes the explicit effect of vertical wind shear on developing clouds and cloud systems. Wind shear plays a crucial role in determining the structure, organization and propagation characteristics of convective clouds and cloud systems, and in the severity of the resulting weather. This critically important effect is missing in convective parameterizations and, likewise, in operational NWP models that use convective parameterization.

We have participated in NWP testing of the ARW model at NCAR, where daily 36 h forecasts have been produced for the spring and summer convective season over the central United States, starting in 2003, using a grid with $\Delta x = 4$ km [9]. This grid spacing is near the upper bound of grid spacings at which explicit simulations of deep convection appear to be feasible [43].

Fig. 6 shows the radar reflectivity for a line of supercell thunderstorms observed at 23 UTC 30 May 2003 along with the 23 h forecast reflectivity from the ARW model valid at that time that was produced as part of the real-time forecast tests [9]. The radar reflectivity for the simulation is diagnosed from the predicted rain, snow, ice and graupel species. These isolated severe storms produced 30 confirmed tornadoes as the line of

Author's personal copy

storms passed through Wisconsin and Illinois, propagating from the west to the east at approximately 18 m/s. The forecast is notable because it predicted a line of strong isolated cells propagating at approximately the same speed as observed with only a small phase error. At present, most operational NWP models do not explicitly simulate individual convective cells, rather, convective parameterizations are used. The parameter-

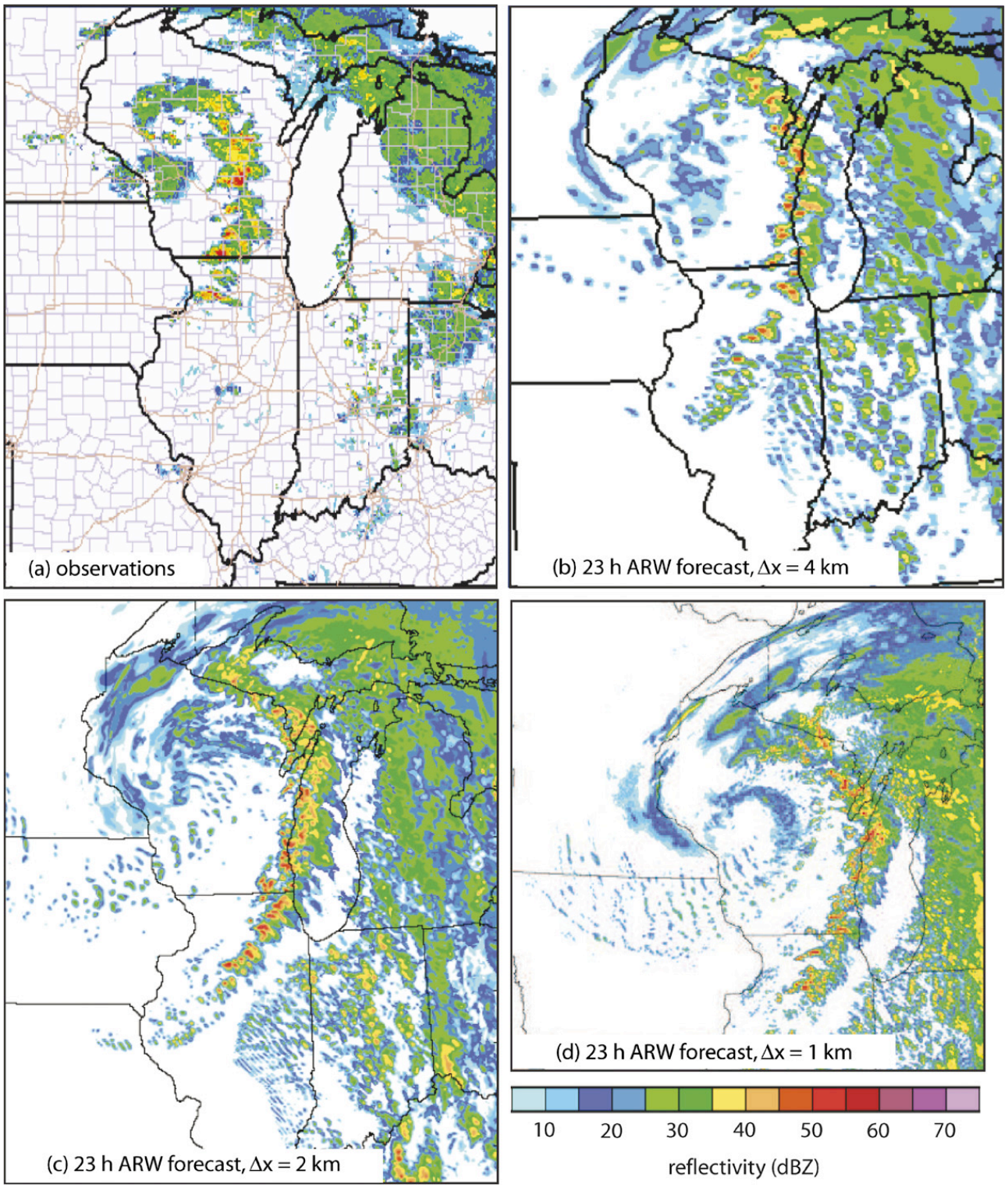

Fig. 6. A line of supercells thunderstorms at 23 UTC 30 May 2003. (a) Observed radar reflectivity. (b) A 23 h forecast from the ARW WRF model using $\Delta x = 4$ km, (c) 23 h forecast using $\Delta x = 2$ km, (d) 23 h forecast using $\Delta x = 1$ km.

Author's personal copy

izations give no indication of the type or severity of convection, and the strong convective line shown in Fig. 6a would appear only as an elongated region of precipitation in operational forecasts.

While the overall structure is well captured in the forecast, there are some noticeable deficiencies in the more detailed features in the forecast. Most obvious is that the simulated reflectivity for the 4 km simulation depicts cells that are significantly larger and stronger than was observed. The 4 km grid also does not allow resolution of some of the defining characteristics of supercell storms, in particular the low-level mesoscyclone (storm-scale cyclonic circulation in the storm, see [18,21]) and propagation to the right of the low-level wind-shear vector (see [18]). Higher resolution does alleviate some of these problems. Fig. 6 also shows results from simulations using $\Delta = 2$ km and 1 km grids for this same forecast (M.L. Weisman, personal communication). The finer grids show convective structure that compares much better to observations than the 4 km forecast as revealed in the reflectivity. The storms exhibit mesocyclones and also are propagating to the right of the low-level shear vector in the 2 and 1 km simulations.

The lifetimes of ordinary convective cells are of the order of 30 min, and supercells may persist for a few hours; hence the convective cells are not deterministically predictable in these 23 h forecasts. From a forecasting perspective, the $\Delta x = 1$ km solution does not offer significantly more information than the $\Delta x = 4$ km solution as the location and propagation of the convective line are quite similar in the two forecasts. Furthermore, recent studies [5] suggest that even higher resolution is needed to resolve individual convective cells and the large eddies responsible for entrainment in the updrafts. In this regard we consider these gridspacings ($\Delta x \sim$ O(1 km)) to be convection-permitting, as opposed to convection-resolving, resolutions.

We have also been testing the capabilities of the ARW model at NCAR in forecasting Atlantic hurricanes. The ARW model has the ability to selectively refine the horizontal grid in rectangular regions. The use of *grid nesting* for hurricane forecasting began in the 1970s [16] and predates the more sophisticated adaptive mesh refinement work (e.g. [7,36]). Fig. 7 shows the observed and forecast radar reflectivity for Hurricane Katrina as it was making landfall just east of New Orleans [42]. Hurricane Katrina was an extremely strong and devastating hurricane that caused billions of dollars (US$) damage as it made landfall on 29 August 2005. This 62 h ARW forecast was produced using a $\Delta x = 12$ km domain within which a $\Delta x = 4$ km refinement automatically tracked the hurricane. The forecast reflectivity captures many significant features of the hurricane, including the areal extent of the hurricane, its banded structure, its intensity, and its notable asymmetries. Consistent with the results from the summer convection experimental forecasts, the simulated reflectivity for the 4 km hurricane simulation depicts cells that are significantly larger and stronger than were observed. Operational hurricane forecast models are not run at grid-spacings that allow the explicit simulation of convective cells – they use convective parameterization. As a result, the operational forecasts do not resolve much of the banded convective structure and entirely miss the more-isolated and sometimes severe (tornado producing) convective cells. Preliminary comparisons of the operational forecasts and the ARW forecasts can be found in [42].

The convective cells and detailed structures in the convective systems shown in these forecasts cannot be compared directly with the observations at the smaller scales – a convective cell lifetime (and predictability timescale) is of order an hour while the simulated time is many tens of hours. In these specific examples, the benefit of explicitly simulating convection is twofold – to gain insight into the character and severity of the convection, and to better simulate the larger-scale effects of the convection, including the vertical transport of heat, moisture, and momentum, the projection of these forcings on the larger scale flow, and the surface precipitation. Whether or not there are objective or subjective benefits of higher resolution, and their relative value versus the costs, are questions being addressed by current research and lead us to examine a number of less traditional verification measures.

3.3. NWP test: statistical measures of solution accuracy

Evaluations of high-resolution NWP forecasts have been largely subjective because the newly appearing small-scale structures (e.g. convective cells) are not deterministically predictable. Traditional verification measures (such as RMS errors) are not meaningful representations of the value and quality of the smaller-scale features resolved in these forecasts because phase errors in these features lead to large errors for these scales in the traditional measures. Accessing the accuracy of model numerics in NWP applications is further com-

Author's personal copy

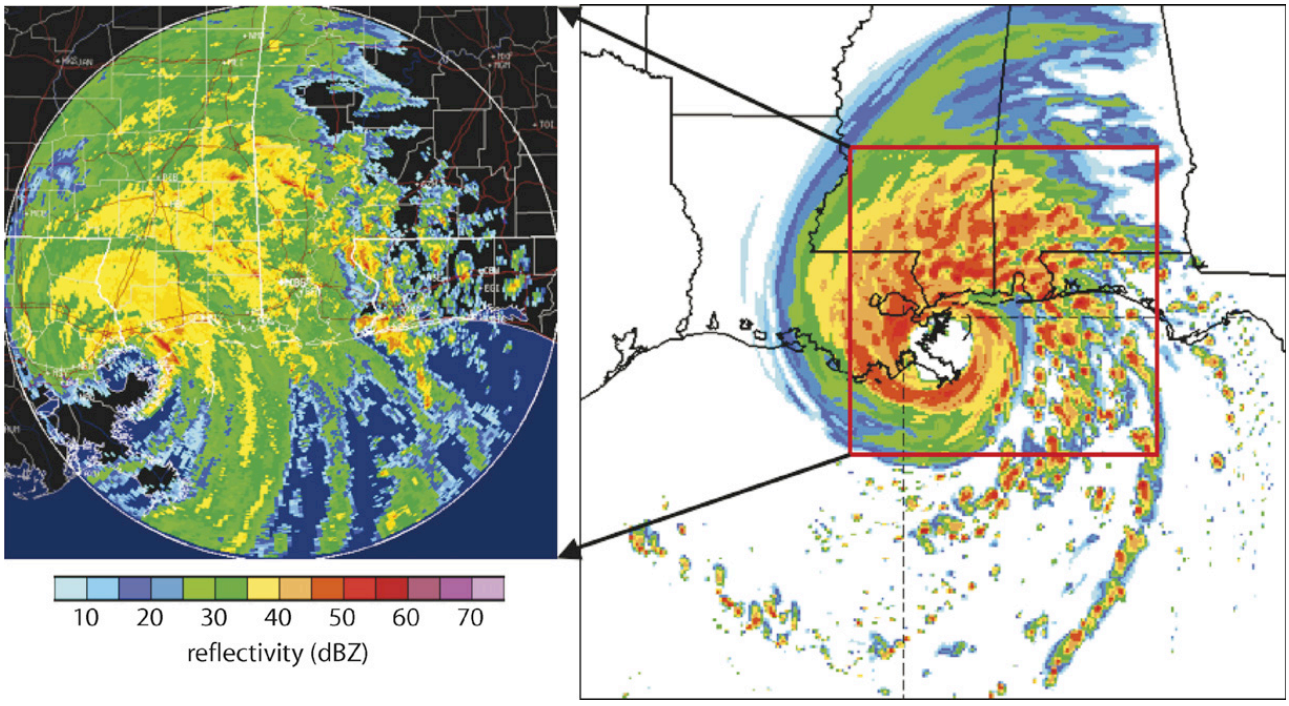

Fig. 7. Observed radar reflectivity (left) from the Mobile Alabama radar for Hurricane Katrina making landfall at 14 UTC 29 August 2005. A 62 h ARW reflectivity forecast valid at that time using $\Delta x = 4$ km.

plicated in that model forecast errors are strongly affected by deficiencies in model initial conditions and physics. We can, however, look at the statistics of the flow and determine whether the statistics related to the small-scale structures are consistent with observations [1]. This provides an additional perspective on verification that addresses the realism of scales represented in the model rather than quantitative accuracy, and allow an assessment of the scale selectivity of dissipation in the model.

Kinetic energy (KE) spectra for the $\Delta x = 4$ km spring–summer 2003 ARW experimental forecasts were examined in [34]. The ARW spectra reproduced the wavenumber dependent transition from $k^{-3} \rightarrow k^{-5/3}$, where k is the wavenumber, that was observed and analyzed [27,23]. The ARW results indicated that the character of the spectra and the transition was largely independent of height in the free troposphere and lower stratosphere. The ARW spectra also showed a sharp dropoff of energy at the highest wavenumbers, indicating where the filters in the model are dissipating energy. The sharp drop-off is not physical – the observed spectra continue to show $k^{-5/3}$ behavior. Model numerics do not correctly represent the smallest wavelengths (2–$6\Delta x$), and removal of energy at these scales is appropriate and important to prevent aliasing to the well-resolved longer wavelengths. We discuss the filters and energy dissipation in models in Section 3.4.

Fig. 8 depicts KE spectra for a two-week period from January 2005 taken from a winter forecast experiment (DWFE [4]) using the ARW model with $\Delta x = 5$ km covering the continental United States. The KE spectra are computed using the approach described in [34]. The winter season weather is characterized by propagating baroclinic waves as opposed to unstable deep convection characteristic of the summer season. Even with the different weather regimes, the winter-season spectra are similar to the summer season spectra. Both show the $k^{-3} \rightarrow k^{-5/3}$ transition at a several hundred kilometer wavelength and a lack of height dependence. There is also a sharp dropoff of energy at wavelength of approximately $7\Delta x$–$8\Delta x$ consistent with the summer season forecast-derived spectra [34].

Since the scale depth of the atmosphere is of order 10 km, the spectral transition and the mesoscale spectrum correspond to two-dimensional flow. There have been a number of hypotheses proposed to explain the transition and the mesoscale character of the spectra (see [23] for a summary), but no conclusive evidence has been presented to confirm any of the candidates. To gain additional insight into the mesoscale spectra, we have decomposed the spectrum from a recent summer-season forecast into rotational, divergent, and deformational components. This is accomplished by decomposing the horizontal velocity fields into a rotational

Author's personal copy

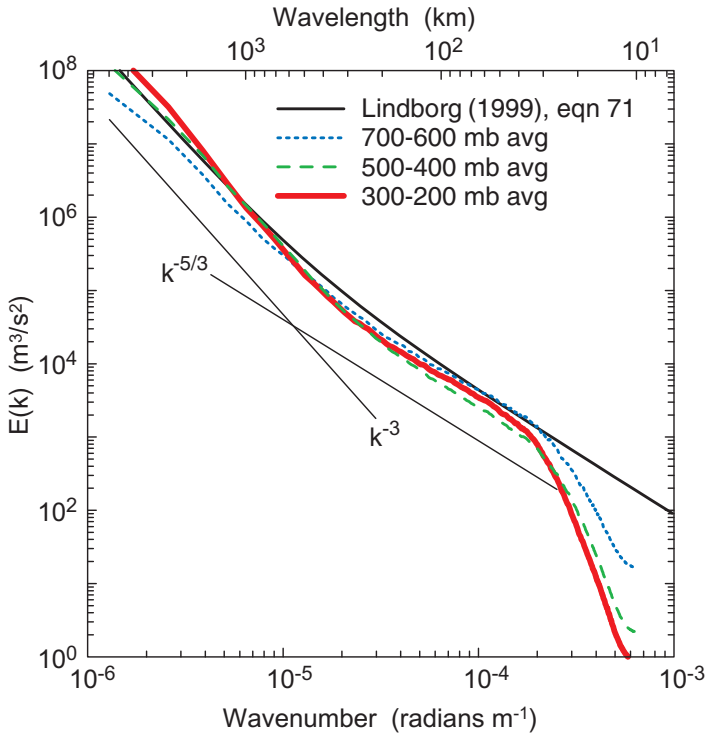

Fig. 8. Kinetic energy spectra from ARW model averaged over 7–25 January 2005 DWFE forecasts for the continental US. The 24, 27, 30, 33, 36, 39, 42, and 45 h forecast spectra were averaged for each daily forecast in this period. The ARW forecasts were produced using $\Delta x = 5$ km.

component V_ψ, a divergent component V_χ, and a deformational component V_{def}, where $V = V_\psi + V_\chi + V_{\text{def}}$. These velocities are defined as:

$$\begin{aligned} V_\psi &= k \times \nabla\psi, \\ V_\chi &= \nabla\chi, \\ V_{\text{def}} &= V - V_\psi - V_\chi, \end{aligned} \tag{25}$$

where

$$\begin{aligned} \nabla^2\psi &= \zeta, \quad \zeta = k \cdot \nabla \times V, \\ \nabla^2\chi &= D, \quad D = \nabla \cdot V, \end{aligned}$$

where k is the unit vector normal to the horizontal coordinate surface. Fig. 9 depicts the results of this decomposition. The energy is dominated by energy in the rotational modes for wavelengths above ~400 km, and the rotational mode spectrum behaves as k^{-3} in this region. Conversely, the divergent mode energy behaves as $k^{-5/3}$ at large scales. For wavelengths less than ~400 km, the rotational and divergent spectra both possess a $k^{-5/3}$ character and have similar energy. This equal partitioning of the energy is an unexpected result that may be due to the simple nature of the decomposition (25), but the results clearly indicate that the divergent component of the energy plays a major role in the spectral transition and the character of the mesoscale spectrum. Many large-scale atmospheric models treat horizontally divergent motions as noise and filter them; those aspects of the formulations are not appropriate for mesoscale simulation if the models are to reproduce the correct velocity variance, energy and enstrophy cascade, and error growth.

Lindborg [23] computed a number of different structure functions using wind measurements from commercial aircraft. One of particular interest related to the turbulent structures in the flow is the kurtosis:

$$\frac{\langle (u_l - u_l(r))^4 \rangle}{\langle (u_l - u_l(r))^2 \rangle^2},$$

Author's personal copy

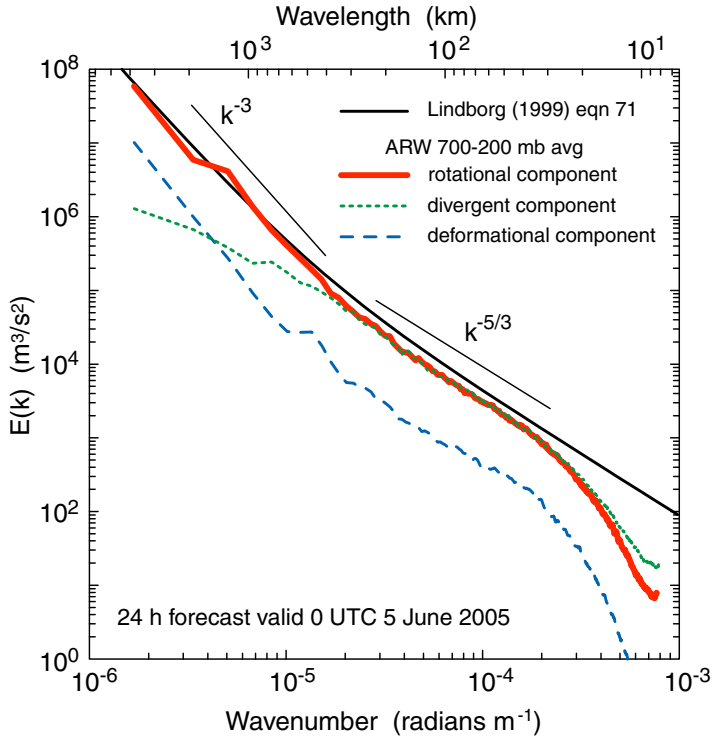

Fig. 9. Decomposed kinetic energy spectra for a spring-season forecast over the continental US. The forecasts were produced using the ARW with $\Delta x = 4$ km.

where r is the distance between the velocities u, and l denotes the velocity component oriented along the line separating the velocities. Fig. 10 shows the kurtosis computed from observations [23] and from a summer season ARW forecast. At large scales both asymptote to a value of approximately 3, which indicates that the velocities have a Gaussian distribution. However, the kurtosis increases dramatically in the mesoscale, indicat-

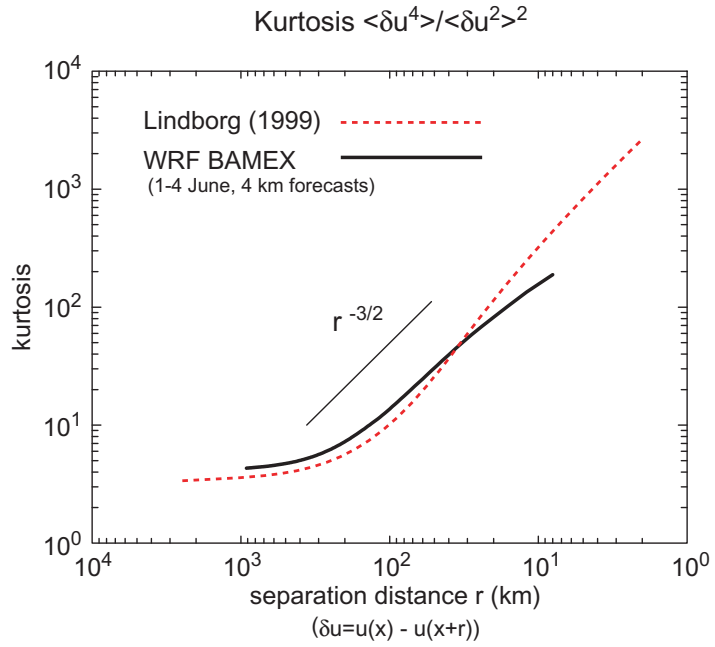

Fig. 10. Kurtosis from observations during the MOZAIC program [23] and from spring forecasts for 1–3 June 2003 over the continental US using the ARW model with $\Delta x = 4$ km.

Author's personal copy

ing strong intermittency in the flow. The transition to strong intermittency occurs at similar length-scales as the spectral transition to $k^{-5/3}$ behavior. Also, the shortest wavelengths in the simulations are damped by the model filters, which produces a shallower slope for wavelengths less than $\sim 7\Delta x$.

3.4. Turbulence and energy dissipation

As noted in the previous section, the ARW KE spectra exhibit a sharp dropoff of energy at the highest wavenumbers, indicating energy dissipation by the model filters. The downscale energy and enstrophy cascades present in atmospheric flows will lead to the artificial buildup (and reflection) of energy and enstrophy at the gridscale in models if energy and enstrophy sinks are not used. It is also well known that wavelengths smaller than $6\Delta x$–$8\Delta x$ are not well resolved by gridpoint models. For example, in most integration schemes $2\Delta x$ waves are stationary and have a group velocity with the wrong sign on an unstaggered grid. These small wavelengths are considered as noise in the solutions and need to be filtered implicitly or explicitly.

For fully three-dimensional turbulence, large eddy simulation (LES) provides for filtering of the small scales using a turbulence parameterization based on 3D turbulence theory [24]. In the atmosphere, LES modeling is used with gridspacings of a few hundred meters or less, where the large eddies in the atmosphere are beginning to be resolved and an inertial subrange appears in the spectra. In the NWP and research simulation results from the previous sections for summer-season convection, hurricanes and winter forecasts, the turbulence is not fully three dimensional. There is no theory to guide subgrid filter design for these scales, and the necessary filtering is usually accomplished in an ad hoc manner based on a subjective determination of when the short waves (noise) have been sufficiently damped while minimally damping the longer waves.

Skamarock [34] advocated using KE spectra to evaluate the damping properties of the filters and found that the KE spectra tails are quite sensitive to the filter design, resolutions, and to a lesser extent weather regimes. Because of this sensitivity, the ARW model uses different filters for different grid spacings, and four different spatial filters are available in the ARW model that can contribute to significant energy dissipation. Parameterizations of turbulent mixing in the planetary boundary layer mix only in the vertical, and the theory on which they are based is valid when the eddies in the boundary layer are not resolved ($\Delta x > \mathrm{O}(1)$ km). This mixing does not directly damp noise with horizontal structure. The ARW model possesses a traditional 3D LES subgrid model that solves a prognostic turbulence energy equation [19] that can be used at LES resolutions ($\Delta x \leqslant \mathrm{O}(100)$ m). The LES subgrid model has often been used with gridspacings of O(1) km, but at these scales the theory on which it is based is not valid and it should be considered more as a numerical filter that depends on local wind shear and buoyancy. A second-order horizontal mixing formulation is also available wherein the mixing coefficient is proportional to the horizontal deformation. While the use of a horizontal-deformation-based mixing coefficient suggests some ties to turbulence in the flow, there is no theoretical basis for this formulation and it should also be considered a purely numerical filter. As noted in Section 2.4, the upwind-biased advection schemes in the ARW solver also provide significant filtering of the small scales. The effective hyperviscosity coefficient is proportional to the Courant number, hence it is most active at higher Courant numbers where phase errors are most likely to produce noise. For NWP applications, we have found that the horizontal mixing provided by the advection scheme using the fifth-order upwind-biased approximation is sufficient to control small-scale noise for grid spacings of $\Delta x \geqslant 10$ km. For grid spacings $1\text{ km} \geqslant \Delta x < 10$ km, we use the horizontal-deformation-based mixing to supplement that from the advection scheme. Unstable convection is explicitly represented on the grid at these resolutions, and the significant input of energy at the gridscale requires stronger filtering. This energy input is handled in a deep-convection parameterization for grids with $\Delta x \geqslant 10$ km by removing the convective instability in vertical columns. Further information on the ARW filters can be found in [33].

The different dissipation mechanisms in the ARW solver are similar in nature to dissipation schemes in other atmospheric NWP and research models, using a mix of both physically based filters and numerical filters. Our formulation does not represent a universal scheme – the available filters are selected and tuned for grid resolutions and flow regimes that, for ARW model applications, span grid spacings Δx from meters to hundreds of kilometers. We know of no solvers that possess optimal solutions to the filtering problem for all scales – an optimal formulation at one resolution or regime often produces over or under damping at

Author's personal copy

another. Sufficient filtering of the smallest, poorly resolved scales, along with model energetics as represented in KE spectra, are important measures of filtering robustness and optimality.

4. Summary

The ARW model is the first fully compressible conservative form nonhydrostatic atmospheric model designed for both research and operational NWP applications. The integration scheme uses time-splitting to handle meteorologically insignificant acoustic modes. The time-splitting allows for efficient integrations for the low-Mach-number flows characteristic of atmospheric flows, and the efficiency of the time-splitting scheme is maintained across a wide range of scales, from synoptic scales where ($\Delta x \sim$ O(100) km), to LES scales where ($\Delta x \sim$ meters). The scheme uses a third-order Runge–Kutta scheme to integrate the slow modes in the Euler equation solver. The spatial discretization uses higher order (fifth) differencing for advection and second-order centered C-grid differencing elsewhere. The vertical coordinate used in the model is the mass (or hydrostatic pressure) coordinate proposed by [20]. The irregular lower boundary of the earth is handled by using the standard terrain-following representation of the mass coordinate.

The mixed order in spatial discretization is justified by the ability of solver to accurately resolve atmospheric structures at resolution limits ($\approx 6\Delta x$–$8\Delta x$). Gravity current test cases comparing fifth-order advection solutions with second-order advection solutions show the advantage of using a high order (fifth) spatial approximation in the advection solver.

Example NWP forecasts for severe storms and hurricanes demonstrate the robustness of the solver where deep unstable convection is explicitly simulated. Using coarse grid spacings for explicit-convection simulations ($\Delta x = 4$ km), realistic convective structure is evident in the forecasts. One of the primary reasons for using fully compressible nonhydrostatic solvers in NWP is that they allow explicit representation of structures previously parameterized (e.g. deep convection). Higher resolution produces better convective system-scale structure and forecasts of these systems than models using completely parameterized convection, even though the convective cells are not deterministically predictable in the high-resolution forecasts.

The robustness and efficiency of solvers is critically dependent on the filters for sub-grid-scale turbulence contained within the solvers. The spectra and kurtosis show the resolution limits of the model and the truncation of the smallest scales on the model grid. These filters may be explicit or implicit within the solver design, and the ARW formulation uses both – an implicit sixth-order filter built into the fifth-order upwind biased advection scheme, and various other explicit filters that are used in different applications. Filter design for resolutions coarser than LES scales ($\Delta x >$ 10's meters) does not have a solid theoretical basis and is necessarily an important development area.

Acknowledgments

Many individuals helped to construct the ARW modeling system in addition to performing many of the simulations shown in this paper. We specifically acknowledge Jimy Dudhia and John Michalakes for their major contributions in designing and constructing the ARW system, and Wei Wang and Morris Weisman for the forecast experiment results shown in this paper.

References

[1] R. Anthes, Regional models of the atmosphere in middle latitudes, Mon. Wea. Rev. 111 (1983) 1306–1335.
[2] P. Bartello, S.J. Thomas, The cost-effectiveness of semi-Lagrangian advection, Mon. Wea. Rev. 124 (1996) 2883–2897, doi:10.1175/1520-0493(1996)124.
[3] R. Benoit, M. Desgagné, P. Pellerin, S. Pellerin, Y. Chartier, S. Desjardins, The Canadian MC2: a semi-Lagrangian, semi-implicit wideband atmospheric model suited for finescale process studies and simulation, Mon. Wea. Rev. 125 (1997) 2382–2415.
[4] L.R. Bernardet, L.B. Nance, H.-Y. Chuang, A. Loughe, M. Demirtas, S. Koch, R. Gall, The developmental testbed center winter forecasting experiment (DWFE). American Meteorological Society, in: 17th Conference on Numerical Weather Prediction, Washington, DC, 31 July–5 August 2005. Available from: <http://www.ametsoc.org>.
[5] G.H. Bryan, J.C. Wyngaard, J.M. Fritsch, Resolution requirements for the simulation of deep moist convection, Mon. Wea. Rev. 131 (2003) 2394–2416.

Author's personal copy

[6] T. Davies, A. Staniforth, N. Wood, J. Thuburn, Validity of anelastic and other equation sets as inferred from normal-mode analysis, Quart. J. Roy. Meteor. Soc. 129 (2003) 2761–2775.
[7] G.S. Dietachmayer, K.K. Droegemeier, Application of continuous dynamic grid adaption techniques to meteorological modeling. Part I. Basic formulation and accuracy, Mon. Wea. Rev. 120 (1992) 1675–1706.
[8] G. Doms, U. Schättler, The Nonhydrostatic Limited-area Model LM (Lokal Modell) of DWD. Part I. Scientific Documentation, Deutscher Wetterdienst (DWD), Offenbach, 1997.
[9] J. Done, C.A. Davis, M.L. Weisman, The next generation of NWP: explicit forecasts of convection using the Weather Research and Forecasting (WRF) Model, Atmos. Sci. Lett. 5 (2004) 110–117.
[10] J. Dudhia, A nonhydrostatic version of the Penn State – NCAR mesoscale model: validation tests and simulation of an Atlantic cyclone and cold front, Mon. Wea. Rev. 121 (1993) 1493–1513.
[11] D.R. Durran, Improving the Anelastic approximation, J. Atmos. Sci. 46 (1989) 1453–1461.
[12] D.R. Durran, J.B. Klemp, A compressible model for the simulation of moist mountain waves, Mon. Wea. Rev. 111 (1983) 2341–2361.
[13] G.J. Haltiner, R.T. Williams, Numerical Weather Prediction and Dynamics Meteorology, second ed., Wiley, New York, 1980, p. 477.
[14] R.M. Hodur, The Naval Research Laboratory's Coupled Ocean/Atmosphere Mesoscale Prediction System (COAMPS), Mon. Wea. Rev. 125 (1997) 1414–1430.
[15] W.B. Hundsdorfer, B. Koren, M. van Loon, J.G. Verwer, A positive finite difference advection scheme, J. Comput. Phys. 117 (1995) 35–46.
[16] R.W. Jones, A nested grid for a three-dimensional model of a tropical cyclone, J. Atmos. Sci. 34 (1977) 1528–1553.
[17] J.B. Klemp, W.C. Skamarock, J. Dudhia, Conservative split-explicit time integration methods for the compressible nonhydrostatic equations, Mon. Wea. Rev. (2007) (in press).
[18] J.B. Klemp, Dynamics of tornadic storms, Annu. Rev. Fluid Mech. 19 (1987) 369–402.
[19] J.B. Klemp, R.B. Wilhelmson, The simulation of three-dimensional convective storm dynamics, J. Atmos. Sci. 35 (1978) 1070–1096.
[20] R. Laprise, The Euler equations of motion with hydrostatic pressure as an independent variable, Mon. Wea. Rev. 120 (1992) 197–207.
[21] L.R. Lemon, C.A. Doswell, Severe thunderstorm evolution and mesocyclone structure as related to tornadogenesis, Mon. Wea. Rev. 107 (1979) 1184–1197.
[22] D.K. Lilly, On the numerical simulation of buoyant convection, Tellus 14 (1962) 148–172.
[23] E. Lindborg, Can the atmospheric kinetic energy spectrum be explained by two-dimensional turbulence? J. Fluid Mech. 388 (1999) 259–288.
[24] C. Meneveau, J. Katz, Scale invariance and turbulence models for large-eddy simulation, Annu. Rev. Fluid Mech. 32 (2000) 1–32.
[25] F. Mesinger, The forward–backward scheme and its use in a limited area model, Contrib. Atmos. Phys. 50 (1977) 200–210.
[26] F. Mesinger, A. Arakawa, Numerical methods used in atmospheric models, GARP Publications Series, No. 17, World Meteorological Organization, 1976.
[27] G.D. Nastrom, K.S. Gage, A climatology of atmospheric wavenumber spectra of wind and temperature observed by commercial aircraft, J. Atmos. Sci. 42 (1985) 950–960.
[28] Y. Ogura, N.A. Phillips, Scale analysis of deep and shallow convection in the atmosphere, J. Atmos. Sci. 19 (1962) 173–179.
[29] K.V. Ooyama, A thermodynamic foundation for modeling the moist atmosphere, J. Atmos. Sci. 21 (1990) 2580–2593.
[30] R.A. Pielke, W.R. Cotton, R.L. Walko, C.J. Tremback, W.A. Lyons, L.D. Grasso, M.E. Nicholls, M.D. Moran, D.A. Wesley, T.J. Lee, J.H. Copeland, A comprehensive meteorological modeling system: RAMS, Meteorol. Atmos. Phys. 49 (1992) 69–91.
[31] R.J. Purser, Accuracy considerations of time-splitting for models using two-time-level schemes, Mon. Wea. Rev. (2007) (in press).
[32] K. Saito, T. Fujita, Y. Yamada, J.-I. Ishida, Y. Kumagai, K. Aranami, S. Ohmori, R. Nagasawa, S. Kumagai, C. Muroi, T. Kato, H. Eito, Y. Yamazaki, The operational JMA nonhydrostatic mesoscale model, Mon. Wea. Rev. 134 (2006) 1266–1298.
[33] W.C. Skamarock, J.B. Klemp, J. Dudhia, D. Gill, D. Barker, W. Wang, J.G. Powers, A description of the Advanced Research WRF Version 2, NCAR Technical Note NCAR/TN-468+STR (2005).
[34] W.C. Skamarock, Evaluating mesoscale NWP models using kinetic energy spectra, Mon. Wea. Rev. 132 (2004) 3019–3032.
[35] W.C. Skamarock, J.B. Klemp, The stability of time-split numerical methods for the hydrostatic and nonhydrostatic elastic equations, Mon. Wea. Rev. 120 (1992) 2109–2127.
[36] W.C. Skamarock, J.B. Klemp, Adaptive grid refinement for two-dimensional and three-dimensional nonhydrostatic atmospheric flow, Mon. Wea. Rev. 121 (1993) 788–804.
[37] J.M. Straka, R.B. Wilhelmson, L.J. Wicker, J.R. Anderson, K.K. Droegemeier, Numerical solutions of a non-linear density current: a benchmark solution and comparisons, Int. J. Numer. Meth. Fluids 17 (1993) 1–22.
[38] A. Staniforth, N. Wood, Aspects of the dynamical core of a nonhydrostatic, deep-atmosphere, unified weather and climate-prediction model, J. Comput. Phys. (2007), doi:10.1016/j.jcp.2006.11.009.
[39] A. Staniforth, J. Côté, Semi-Lagrangian integration schemes for atmospheric models: a review, Mon. Wea. Rev. 119 (1991) 2206–2223.
[40] M.C. Tapp, P.W. White, A non-hydrostatic mesoscale model, Quart. J. Roy. Meteor. Soc. 102 (1976) 277–296.
[41] S.C. Thomas, C. Girard, G. Doms, U. Schättler, Semi-implicit scheme for the DWD Lokal-Modell, Meteorol. Atmos. Phys. 73 (2000) 105–125.
[42] W. Wang, C. Davis, J.B. Klemp, G. Holland, M. DeMaria, Evaluation of WRF-ARW high-resolution tropical storm forecasts in the 2005 season, American Meteorological Society, in: 27th Conference on Hurricanes and Tropical Meteorology, Monterey, CA, 23–28 April 2006. Available from: <http://www.ametsoc.org>.
[43] M.L. Weisman, W.C. Skamarock, J.B. Klemp, The resolution dependence of explicitly modeled convective systems, Mon. Wea. Rev. 125 (1997) 527–548.

Author's personal copy

[44] L.J. Wicker, W.C. Skamarock, Time splitting methods for elastic models using forward time schemes, Mon. Wea. Rev. 130 (2002) 2088–2097.
[45] M. Xue, K.K. Droegemeier, V. Wong, The Advanced Regional Prediction System (ARPS) – a multiscale nonhydrostatic atmospheric simulation and prediction tool. Part I. Model dynamics and verification, Meteor. Atmos. Phys. 75 (2000) 161–193.
[46] K.-S. Yeh, J. Côté, S. Gravel, A. Méthot, A. Patoine, M. Roch, A. Staniforth, The CMC-MRB Global Environmental Multiscale (GEM) Model. Part III. Nonhydrostatic formulation, Mon. Wea. Rev. 130 (2002) 339–356.